PHYSICAL REVIEW C, VOLUME 63, 064606

Threshold anomaly in the $^{19}\mathrm{F}+^{208}\mathrm{Pb}$ system

C. J. Lin, J. C. Xu, H. Q. Zhang, Z. H. Liu, F. Yang, and L. X. Lu
China Institute of Atomic Energy, P.O. Box 275(10), Beijing 102413, China

(Received 26 October 2000; published 11 May 2001)

Angular distributions of elastic scatterings for the $^{19}\mathrm{F}+^{208}\mathrm{Pb}$ system were measured at six energies around the Coulomb barrier. By means of a phenomenological optical model analysis, it is found that the real and imaginary potentials show a pronounced energy dependence. The real parts of potentials extracted from the fusion data are similar to those from the elastic data. A comparison with the neighboring systems of $^{16}\mathrm{O}+^{208}\mathrm{Pb}$ and $^{16}\mathrm{O}+^{209}\mathrm{Bi}$ reveals that the effects of the $^{19}\mathrm{F}$ deformations in the entrance channel play an important role in the fusion reaction. Based on the deformed and energy dependent barrier penetration model, the calculation results of the fusion cross sections and mean-square spin distribution agree with the experimental data well. Furthermore, it is indicated that the enhancement of fusion cross sections is attributed to the dynamic polarization effects around the barrier, and to the static deformation effects further below the barrier.

DOI: 10.1103/PhysRevC.63.064606 PACS number(s): 25.70.Bc, 25.70.Jj

I. INTRODUCTION

Since the early 1980's, it has been gradually recognized that the coupled-channels (CC) effects play important roles in the heavy ion reactions at the energies around the Coulomb barrier. Some interesting phenomena, such as the threshold anomaly (TA) [1–3], the enhancement of fusion cross sections, the broadening of compound nuclei spin distribution [4–6], the barrier distribution [7–9], etc., have been extensively studied and are well understood. Generally speaking, the CC calculations can reproduce these phenomena. Very recently the CC description has met a severe challenge. For example, it has been reported that the experimental barrier distribution and the fusion cross sections cannot be simultaneously described by the CC theory for the typical system of $^{16}\mathrm{O}+^{208}\mathrm{Pb}$ [10]. Indeed, the CC calculation results are sensitive not only to the number of coupled channels, but also to the strength of individual channel and the potential parameters, even in the case of coupling to weak channels. In other words, some uncertainties exist in the CC calculations. Although it is known that the TA phenomenon comes from the CC effects and exhibits the gross feature in the elastic channel, this phenomenon still needs to be investigated. Until now, most systems studied have been spherical or near spherical ones. Very little work has been done for well deformed systems [11] with an attempt to understand the effects of the nuclear structure, especially for the systems with deformed projectile. In this work, the $^{19}\mathrm{F}+^{208}\mathrm{Pb}$ system was chosen because $^{19}\mathrm{F}$ nucleus has quite large static deformations ($\beta_2=0.44,\beta_4=0.14$) [12]. The CC effects in this system should be pronounced due to the deformations and appreciably influence the fusion channels. Since TA in the neighboring systems of $^{16}\mathrm{O}+^{208}\mathrm{Pb}$ and $^{16}\mathrm{O}+^{209}\mathrm{Bi}$ is well established, it is interesting to make a comparison with these systems. Furthermore, the fusion data of $^{19}\mathrm{F}+^{208}\mathrm{Pb}$ system are available in the literature. It is meaningful to compare the data with the calculations of the barrier penetration model (BPM) modified by the deformations and energy dependence.

The TA phenomenon can be understood as follows: The absorptive potential decreases with the effective close of the nonelastic channels when the energy decreases, hence the threshold of the imaginary part of potential $[W(r;E)]$ emerges; meanwhile, the real part of potential $[V(r;E)]$ a rapid variation occurs according to the causality principle. This is the so-called threshold anomaly. The interaction potential can be written in the complex form

$$U(r;E)=V(r;E)+iW(r;E), \tag{1}$$

where $V(r;E)$ is divided into two parts

$$V(r;E)=V_0(r;E)+\Delta V(r;E). \tag{2}$$

The term $V_0(r;E)$ is slowly and smoothly energy dependent which arises from the nonlocality effects, namely, ‘‘spurious’’ E dependence [3]. The second term $\Delta V(r;E)$ is a consequence of the causality principle and links to $W(r;E)$ with the dispersion relation

$$\Delta V(r;E)=\frac{P}{\pi}\int_0^\infty \frac{W(r;E')}{E'-E}\,dE'. \tag{3}$$

Here P is the integrated principal value. From the dispersion relation it is immediately known that any localized variation of the imaginary potential will result in a localized variation of the real potential. This standpoint is important to the later analysis.

The present paper is organized as follows. In Sec. II we briefly describe the experimental procedure. Section III explicitly introduces the optical model analysis and the way to extract the TA parameters from the elastic scatterings. The polarization potentials extracted from the fusion excitation function are also included in this section. The comparison with the neighboring systems, the calculations of fusion cross sections, and mean-square spin distribution are presented in Sec. IV. The summary is included in Sec. V.

II. THE EXPERIMENT

The experiment was carried out at HI-13 tandem accelerator of China Institute of Atomic Energy, Beijing. A $^{208}\mathrm{Pb}$ target of thickness about 100 $\mu\mathrm{g/cm}^2$ evaporated on a 20 $\mu\mathrm{g/cm}^2$ carbon foil backing was bombarded by a collimated $^{19}\mathrm{F}$ beam. The beam energies were 88, 91, 93, 96, 98,

0556-2813/2001/63(6)/064606(7)/$20.00

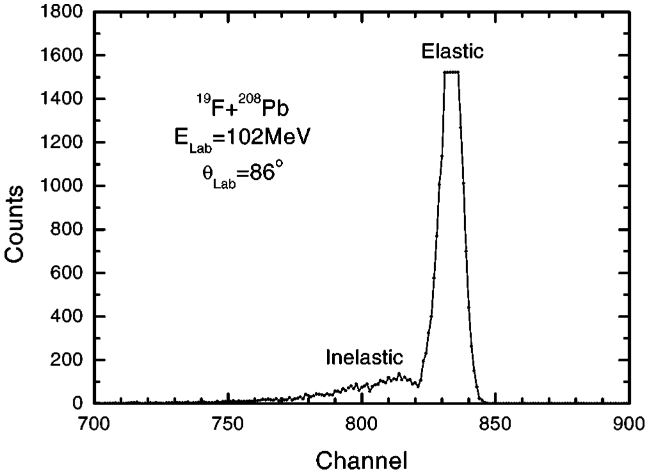

FIG. 1. A typical elastic and inelastic spectrum at $E_{\mathrm{lab}} = 102$ MeV and $\theta_{\mathrm{lab}} = 86°$ for the $^{19}\mathrm{F} + ^{208}\mathrm{Pb}$ system.

and 102 MeV, respectively. The beam current range was 100–300 enA. The reaction products were detected by three pairs of ΔE-E telescope counters with a total energy resolution less than 1.3%. A typical spectrum cut by the $Z = 9$ banana in the ΔE-E matrix is shown in Fig. 1 at $E_{\mathrm{lab}} = 102$ MeV and $\theta_{\mathrm{lab}} = 86°$. The laboratory angle range was from 40° to 160° in 4° intervals. A Si(Au) surface barrier detector was mounted at $-42.4°$ with respect to the beam direction as a monitor to detect the elastic scatterings. All the reaction cross sections were normalized to the monitor counts, assuming that the elastic cross sections equal to the Rutherford cross sections at the forward angles.

The energy resolution of the detectors allows one to separate all the $E_x \geqslant 1.3457$ MeV states of ^{19}F and all the excitation states of ^{208}Pb from ground state, while the two lower excitation states 0.10989 and 0.19714 MeV of ^{19}F cannot be resolved from the measured elastic scatterings. Thus the elastic spectra include the inelastic scatterings of these two low-lying excitation states. The elastic scattering cross sections normalized to the Rutherford cross sections for all energies are shown in Fig. 2. The overall error is 3% for the forward angles and gradually increases to 10% for the backward angles. A few points have more than 10% errors at the backward angles due to the low statistic.

III. ENERGY DEPENDENT POTENTIALS

A. Optical model analysis of elastic scatterings

Most authors made use of both phenomenological and microscopic analyses to get the polarization potentials. The same results were obtained with these two approaches. In this work the phenomenological optical potentials are utilized only. Since the low-lying excited states are not resolved, the coupled-channels code ECIS95 [13] is employed to fit the elastic scattering angular distributions in order to get the pure elastic scattering potentials. In these calculations only the couplings between the $E_x = 0.19714$ MeV, $J^\pi = \frac{5}{2}^+$ state and ground state, which belong to the $K = \frac{1}{2}^+$ ground state rotational band, are taken into account. The same optical potentials are assumed for these two coupling nuclear states. Another excitation state $E_x = 0.10989$ MeV, $J^\pi = \frac{1}{2}^-$ which belongs to $K = \frac{1}{2}^-$ band is not included, because the strength coupled to the ground state band is very weak. The potential is defined as

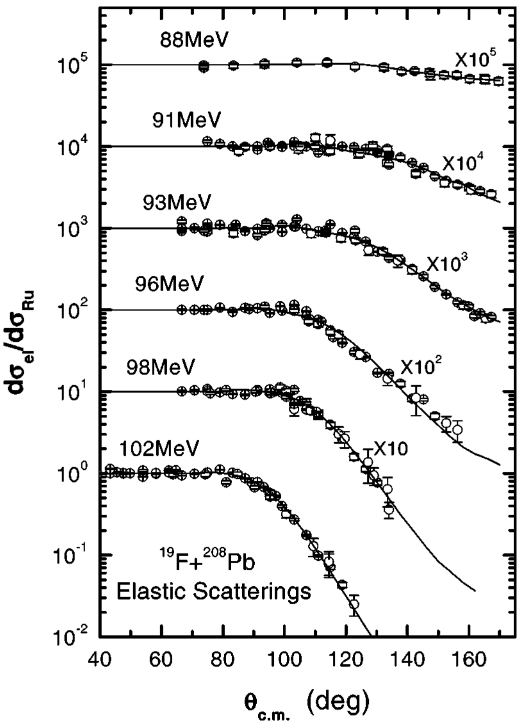

FIG. 2. Elastic scattering angular distributions for the $^{19}\mathrm{F} + ^{208}\mathrm{Pb}$ system at different laboratory energies. The solid lines are optical model fits by the ECIS code with $r_0 = 1.24$ fm and $a_0 = 0.53$ fm.

$$V(r) = V_C(r) + V_N(r). \tag{4}$$

Here $V_C(r)$ is the Coulomb potential

$$V_C(r) = \begin{cases} (3R_C^2 - r^2)Z_1Z_2e^2/(2R_C^3), & r < R_C, \\ Z_1Z_2e^2/r, & r \geqslant R_C, \end{cases} \tag{5}$$

where $R_C = r_{0c}(A_1^{1/3} + A_2^{1/3})$ with r_{0c} fixed at 1.33 fm. Corresponding to Eq. (1), the nuclear potential $V_N(r)$ is composed of two parts

$$V_N(r) = V(r) + iW(r) = V_0 f_v(r) + iW_0 f_w(r), \tag{6}$$

where V_0 and W_0 are the depths of the real and imaginary parts of the potentials with Woods-Saxon form

$$f_i(r) = [1 + \exp\{(r - R_i)/a_i\}]^{-1}, \tag{7}$$

where $R_i = r_{0i}(A_1^{1/3} + A_2^{1/3})$ and $i = v, w$, respectively.

In the present analysis, the geometrical shapes of the real and imaginary potentials are kept the same ($r_{0v} = r_{0w} = r_0$, $a_v = a_w = a_0$). In order to assess the influences of the potential parameters, two sets of fits are performed with the fixed radius parameters $r_0 = 1.20$ and $r_0 = 1.24$ fm, respectively. For each set, a grid search is made on the diffuseness parameters ($a_0 = 0.43$, 0.48, 0.53, 0.58, 0.63, 0.68 fm)

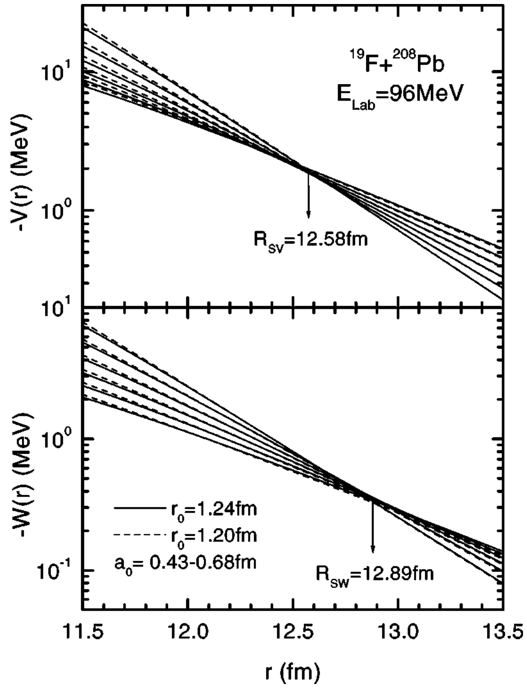

FIG. 3. The real and imaginary parts of the Woods-Saxon optical potentials with different geometric shapes to fit the elastic scattering angular distribution at $E_{\mathrm{lab}}=96$ MeV. The solid and dashed lines are fits with $r_0=1.20$ fm and $r_0=1.24$ fm, respectively. The diffuseness parameters vary from 0.43 fm to 0.68 fm for both solid and dashed lines.

to obtain the best V_0 and W_0 values with the minimum χ^2. As an example, Fig. 3 illustrates the real and imaginary potentials obtained in these fits at $E_{\mathrm{lab}}=96$ MeV. The solid and dashed lines represent these two sets with $r_0=1.20$ and $r_0=1.24$ fm, respectively. All the lines converge at a certain distance, namely sensitive radius (R_S). At the sensitive radius, the potentials have a minimum uncertainty and are nearly independent on geometrical shapes. As pointed out by Macfarlane and Pieper [14], the sensitive radius is close to the classical strong absorption radius $D_{1/2}$. For example, the strong absorption radius $D_{1/2}$ is 12.75 fm at $E_{\mathrm{lab}}=96$ MeV for ^{19}F+^{208}Pb system. It is realized that the R_S values depend on the energies and have some differences between the real and imaginary parts of potentials, as listed in Table I. In the $E_{\mathrm{lab}}=88$ MeV case, the lines are too divergent to define a good R_S for the imaginary parts of potentials. The R_{SV} varies from 12.2 to 12.9 fm and R_{SW} from 12.1 to 13.2 fm, monotonously depending on the energies in this energy range. For consistency, $R_S=12.5$ fm for both real and imaginary parts of potentials are taken for all energies. The χ^2's of the fits reach the minimum values when $r_0=1.24$ fm and $a_0=0.53$ fm for all energies. The results of the best fits in this case are also listed in Table I. The real and imaginary parts of potentials at the sensitive radius (V_S and W_S) are illustrated in Fig. 4 with the circle symbols. The errors are derived from the χ^2 values. The figure shows clearly that the potentials are energy dependent around the Coulomb barrier, as the same behavior as the typical TA.

TABLE I. The sensitive radii and the results of the best fits obtained at $r_0=1.24$ and $a_0=0.53$ fm for elastic scatterings.

E_{lab} (MeV)	R_{SV} (fm)	R_{SW} (fm)	$-V_0$ (MeV)	$-W_0$ (MeV)	χ^2/pt	σ_R (mb)
102	12.86	13.16	73.2	44.5	7.67	1169.
98	12.62	12.75	77.2	23.4	10.5	897.2
96	12.58	12.89	77.5	22.5	27.1	838.3
93	12.50	12.20	85.1	10.2	14.2	673.2
91	12.32	12.12	88.6	3.44	8.87	579.9
88	12.24		78.4	1.57	1.25	512.0

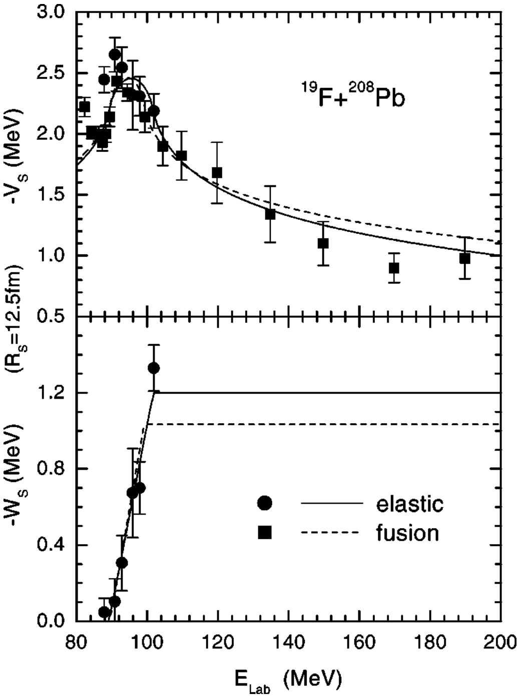

FIG. 4. The real and imaginary potentials at $R_S=12.5$ fm are plotted as a function of E_{lab}. The circle (or solid) and square (or dashed) symbols (or lines) represent the results obtained from elastic scattering and fusion analyses, respectively.

B. Extract TA parameters in linear model

For convenience, the linear schematic model of the two straight line segments is utilized to describe the TA (see Refs. [2,3] for details). $W_S(E)$ is defined as

$$W_S(E)=\begin{cases} 0, & E\leqslant E_a, \\ W_{0S}\dfrac{E-E_a}{E_b-E_a}, & E_a<E<E_b, \\ W_{0S}, & E\geqslant E_b, \end{cases} \tag{8}$$

and the V_S is

$$\begin{aligned} V_S(E)&=V_{0S}+\Delta V_S(E)\\ &=V_{0S}-(W_{0S}/\pi)[\varepsilon_a \ln|\varepsilon_a|-\varepsilon_b \ln|\varepsilon_b|], \end{aligned} \tag{9}$$

according to Eq. (2) and Eq. (3). Here $\varepsilon_i=(E-E_i)/(E_b\varepsilon_i=(E-E_i)/(E_b-E_a)$ with $i=a,b$, respectively. In the above equations the variables with subscript S indicate the values at the sensitive radius. Thus, in the linear model the behavior of TA can be described by four parameters E_a, E_b, W_{0S}, and V_{0S}.

In general, the TA parameters, except V_{0S}, are determined by fitting the imaginary potentials with Eq. (8), and the V_{0S} is obtained at the reference point of which the real potential is almost energy independent. Due to the energy limit, the present work lacks some high-energy points as references to extract the energy-independent potential W_{0S}. Moreover, no elastic scattering data in the literature are available for this system. Anyway the real and imaginary potentials can be simultaneously fit by Eqs. (8) and (9), assuming the dispersion relation is tenable (assuredly, this assumption is trustworthy). Thus the four parameters $E_a=89.2$ MeV, $E_b=101.7$ MeV, $W_{0S}=-1.20$ MeV, and $V_{0S}=-2.19$ MeV were reliably extracted by the fits. The results are shown in Fig. 4 with the solid lines.

C. Extract TA parameters from fusion data

In fact, the energy dependent potentials can be extracted from the fusion excitation function. It is interesting to compare them with those from elastic scatterings. In the following calculations, the BPM model with deformation correction is used, and the symmetrical deformations of ^{19}F up to hexadecapole are taken into account on the basis of Wong model [15]. The radial radius is expressed as

$$R(\theta)=R_0[1+\beta_2Y_2(\theta)+\beta_4Y_4(\theta)]. \tag{10}$$

Here R_0 is the radius of the spherical nucleus with equivalent volume, θ is the orientation angle of deformed nucleus with respect to the collision axis, and the $Y_i(\theta)$ is the spherical harmonic. Now the total interaction potential becomes

$$V(r,\theta)=V_C(r,\theta)+V_N(r,\theta), \tag{11}$$

where the Coulomb potential

$$\begin{aligned}V_C(r,\theta)=\frac{Z_1Z_2e^2}{r}\Bigg\{1&+\frac{1}{r^2}\sum_{i=P,T}R_{0i}^2\Bigg[\sqrt{\frac{9}{20\pi}}\beta_{2i}P_2(\cos\theta_i)\\&+\frac{3}{7\pi}[\beta_{2i}P_2(\cos\theta_i)]^2\Bigg]\\&+\frac{1}{r^4}\sum_{i=P,T}R_{0i}^4\sqrt{\frac{1}{4\pi}}\beta_{4i}P_4(\cos\theta_i)\Bigg\},\end{aligned} \tag{12}$$

and the nuclear potential

$$\begin{aligned}V_N(r,\theta)=V_0\Bigg[1+\exp\Bigg\{\Bigg(r-R_0&\\-\sum_{i=P,T}R_{0i}\Bigg[\sqrt{\frac{5}{4\pi}}\beta_{2i}P_2(\cos\theta_i)&\\+\sqrt{\frac{9}{4\pi}}\beta_{4i}P_4(\cos\theta_i)\Bigg]\Bigg)/a\Bigg\}\Bigg]^{-1}&,\end{aligned} \tag{13}$$

with

$$R_0=R_{0P}+R_{0T}+0.29\ \text{fm},$$

$$R_{0i}=(1.233A_i^{1/3}-0.98A_i^{-1/3})\ \text{fm},$$

and the diffuseness parameter $a=0.63$ fm. $P(\cos\theta)$ is the Legendre polynomial, and $i=P,T$ which denote the projectile and target, respectively. The orders of Legendre polynomial are considered up to 4, neglecting the higher order terms and other square terms. The nuclear potential contains only the real part of potential with Woods-Saxon form. The initial value is estimated in terms of proximate potential [16]

$$V_0=16\pi\gamma\overline{R}a\ \text{MeV}, \tag{14}$$

with

$$\gamma=0.95\left[1-1.8\left(\frac{N_P-Z_P}{A_P}\right)\left(\frac{N_T-Z_T}{A_T}\right)\right]\text{MeV fm}^{-2}, \tag{15}$$

and $\overline{R}=R_{0P}R_{0T}/(R_{0P}+R_{0T})$. The fusion cross sections are calculated by the BPM model under the parabolic approximation. The partial cross section at each angle is given by

$$\begin{aligned}\sigma_f^l(E,\theta)=\frac{\pi(2l+1)}{k^2}\Bigg[1+\exp\Bigg\{\frac{2\pi}{\hbar\omega(\theta)}\Bigg(V_B(\theta)-E_{\text{c.m.}}&\\+\frac{l(l+1)\hbar^2}{2\mu R_B^2(\theta)}\Bigg)\Bigg\}\Bigg]^{-1}&,\end{aligned} \tag{16}$$

where k is the wave number, μ is the reduced mass, $V_B(\theta)$, $R_B(\theta)$, and $\hbar\omega(\theta)$ the barrier parameters (height, radius, and curvature) for different orientations. The cross section at each angle is given by

$$\begin{aligned}\sigma_f(E,\theta)&=\sum_l\sigma_f^l(E,\theta)\\&=\frac{R_B^2(\theta)\hbar\omega(\theta)}{2E_{\text{c.m.}}}\ln\Bigg[1+\exp\Bigg\{\frac{2\pi}{\hbar\omega(\theta)}[E_{\text{c.m.}}\\&\quad-V_B(\theta)]\Bigg\}\Bigg].\end{aligned} \tag{17}$$

Finally, the total cross section is given by integration over the angles

$$\sigma_f(E)=\int_0^{\pi/2}\sigma_f(E,\theta)d\theta. \tag{18}$$

In terms of Eqs. (11)–(18), the real potential depth, V_0 can be extracted from the experimental fusion cross sections. The results are listed in Table II. The barrier parameters ($\overline{V_B}$, $\overline{R_B}$, and $\hbar\overline{\omega}$) averaged over the angle θ are also listed in the same table. The errors are determined by the largest deviations of experimental fusion cross sections taken from the literature [17,18]. In order to compare with the TA be-

TABLE II. The barrier parameters and the best real potentials for the experimental fusion cross sections at $R=R_P+R_T+0.29$ fm and $a_0=0.63$ fm.

E_{lab} (MeV)	σ_f [a] (mb)	$\overline{V_B}$ (MeV)	$\overline{R_B}$ (fm)	$\hbar\overline{\omega}$ (MeV)	$-V_0$ (MeV)
82.32	0.15±0.03	83.91±0.18	11.95±0.03	4.60±0.01	69.24±2.42
84.32	0.91±0.11	84.43±0.12	11.87±0.02	4.57±0.01	62.55±1.43
86.32	5.30±0.55	84.46±0.16	11.86±0.03	4.57±0.01	62.24±1.84
87.32	8.83±0.90	84.65±0.18	11.83±0.03	4.56±0.01	60.02±2.05
88.33	16.32±1.3	84.44±0.18	11.87±0.03	4.57±0.01	62.39±2.07
89.33	28.23±2.0	84.10±0.18	11.92±0.03	4.59±0.01	66.64±2.35
91.34	69.01±3.8	83.46±0.16	12.03±0.03	4.62±0.01	75.77±2.36
94.35	159.6±8.0	83.65±0.16	12.00±0.03	4.61±0.01	72.95±2.27
99.38	350.2±17.5	84.10±0.30	11.92±0.05	4.59±0.02	66.68±4.02
104.37	509.6±25.5	84.72±0.43	11.82±0.07	4.55±0.04	59.18±4.98
109.74	685.0±35.0	84.95±0.57	11.78±0.10	4.53±0.06	56.63±6.29
119.75	965.0±50.0	85.37±0.76	11.71±0.13	4.49±0.09	52.47±7.79
134.77	1245.0±65.0	86.66±0.92	11.49±0.17	4.31±0.20	41.78±7.13
149.78	1440.0±75.0	87.92±0.98	11.26±0.19	4.01±0.39	34.15±5.73
169.79	1615.0±80.0	89.33±0.88	10.96±0.20	3.32±0.50	27.96±3.58
189.81	1910.0±95.0	88.65±1.05	11.11±0.22	3.72±0.64	30.63±5.17

[a] The fusion cross sections of energies between 82.32 and 104.37 MeV were taken from Ref. [18]. The others were taken from Ref. [17].

havior of elastic scatterings, the V_S values are calculated at the same sensitive radius 12.5 fm, and the results are also shown in Fig. 4 with the square symbols. In the figure, the dashed line in the real part of potentials represents the best fit of the extracted V_S by Eq. (9) with TA parameters $E_a=89.5$ MeV, $E_b=99.1$ MeV, $W_{0S}=-1.03$ MeV, and $V_{0S}=-2.23$ MeV. The dashed line in the imaginary part of potentials is the results calculated by Eq. (8). It should be pointed out that the potentials extracted from the fusion data correspond to the inner radius and it has a large degree of uncertainty to extrapolate to an outer radius, for example, to the sensitive radius. Anyhow, it can be seen from the figure that these two kinds of TA behavior are similar. This reflects that both of them are caused by the CC effects.

IV. DISCUSSIONS AND CONCLUSIONS

A. Comparison with ^{16}O+^{208}Pb and ^{16}O+^{209}Bi systems

It is interesting to compare the present findings of ^{19}F+^{208}Pb system with the existing results of ^{16}O+^{208}Pb and ^{16}O+^{209}Bi systems. The reaction, quasielastic and fusion cross sections as a function of $E_{\mathrm{c.m.}}-V_B$ for these three systems are plotted in Fig. 5. The data of ^{16}O+^{208}Pb and ^{16}O+^{209}Bi systems are taken from Refs. [19–21]. Here the Bass barriers [22] of 85.4, 77.1, and 78.0 MeV are used for ^{19}F+^{208}Pb, ^{16}O+^{208}Pb, and ^{16}O+^{209}Bi systems, respectively. As shown in Fig. 5, both reaction and quasielastic cross sections are comparable for the ^{16}O+^{208}Pb and ^{16}O+^{209}Bi systems, while obviously larger for the ^{19}F+^{208}Pb system. Maybe, the larger probability of the quasielastic reactions results from the structure of projectile ^{19}F. The fusion cross sections are comparable for these three systems at near and well above barrier energies, but at energies lower than a

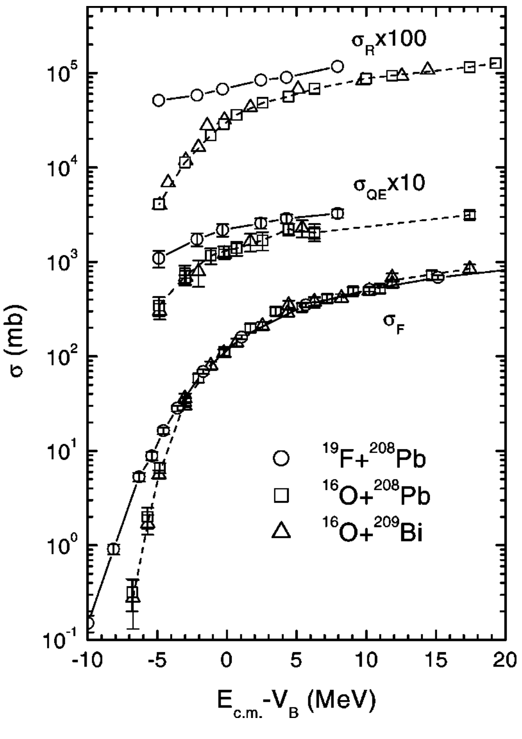

FIG. 5. The comparison of the reaction (σ_R), quasielastic (σ_{QE}), and fusion (σ_F) cross sections for the ^{19}F+^{208}Pb (circle), ^{16}O+^{208}Pb (square), and ^{16}O+^{209}Bi (triangle) systems. The solid and dashed lines are to guide the eye for ^{19}F+^{208}Pb and ^{16}O+^{208}Pb systems, respectively.

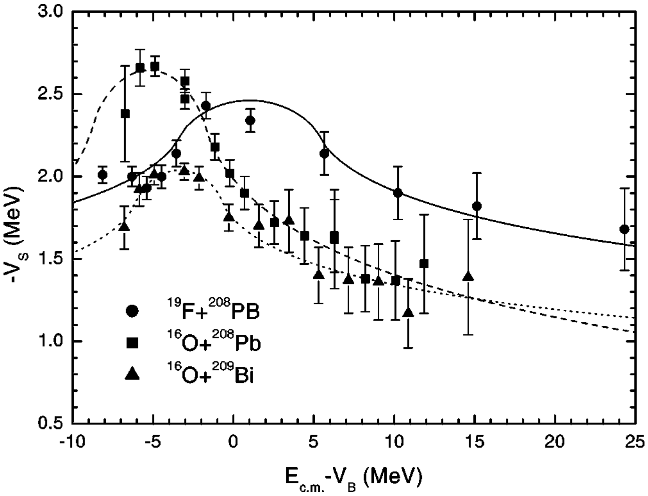

FIG. 6. Comparison of the real potentials at sensitive radii for the ^{19}F+^{208}Pb (circle), ^{16}O+^{208}Pb (square), and ^{16}O+^{209}Bi (triangle) systems, respectively. The solid, dashed, and dotted lines are fitted by Eq. (9) for these three systems, respectively.

certain value (i.e., 3 MeV below the barrier) the fusion cross sections of ^{19}F+^{208}Pb system are obviously larger than those of the other two which are still comparable. The real potentials of these systems are extracted with the method mentioned above, as shown in Fig. 6. The sensitive radii are taken as 12.5, 12.4, and 12.5 fm for ^{19}F+^{208}Pb, ^{16}O+^{208}Pb, and ^{16}O+^{209}Bi systems, respectively. The solid, dashed, and dotted lines are the results fitted with Eq. (9) for ^{19}F+^{208}Pb, ^{16}O+^{208}Pb, and ^{16}O+^{209}Bi systems, respectively. The TA parameters of these three systems are listed in Table III for comparison. The anomaly behaviors of ^{16}O+^{208}Pb and ^{16}O+^{209}Bi systems are also similar to those extracted from elastic channels [2,21]. As shown in Fig. 6 and Table III, the anomaly peaks locate around the barrier for ^{19}F+^{208}Pb system but below the barrier for ^{16}O+^{208}Pb and ^{16}O+^{209}Bi systems. The anomaly centers $[E_{1/2}=(E_a+E_b)/2-V_B]$ are 1.01, -5.26, and -3.38 MeV and the anomaly intensities $[\Delta V_{\max}=\Delta V(E_{1/2})-\Delta V(E_S)]$ are about 1.0, 1.6, and 0.9 MeV for ^{19}F+^{208}Pb, ^{16}O+^{208}Pb, and ^{16}O+^{209}Bi systems, respectively. Here E_S is the reference energy chosen to be 30 MeV higher than the Coulomb barrier. It is difficult to understand why ^{16}O+^{208}Pb and ^{16}O+^{209}Bi systems have the same tendencies in fusion excitation function while ^{19}F+^{208}Pb system does not. Moreover, as shown in Refs. [3,21], the fusion excitation functions can be reproduced by considering the energy dependent potentials for ^{16}O+^{208}Pb and ^{16}O+^{209}Bi systems. But for ^{19}F+^{208}Pb system, the following analysis shows that it is not enough to explain the larger fusion cross sections at low energies. When the effects of ^{19}F deformations are also taken into account in the calculations, the fusion excitation function can be reproduced quite well. Hence, we may conclude that the nuclear deformations give rise to some effects in the process of fusion below the Coulomb barrier.

TABLE III. TA parameters for the ^{19}F+^{208}Pb, ^{16}O+^{208}Pb, and ^{16}O+^{209}Bi systems.

System	^{19}F+^{208}Pb	^{16}O+^{208}Pb	^{16}O+^{209}Bi
$-V_{0S}$ (MeV)	2.23±0.05	2.30±0.07	1.85±0.05
$-W_{0S}$ (MeV)	1.03±0.08	1.59±0.03	0.84±0.16
E_a-V_B(MeV)	-3.39±0.62	-8.80±2.52	-6.02±0.71
E_b-V_B(MeV)	5.42±0.96	-1.72±0.58	-0.73±0.87

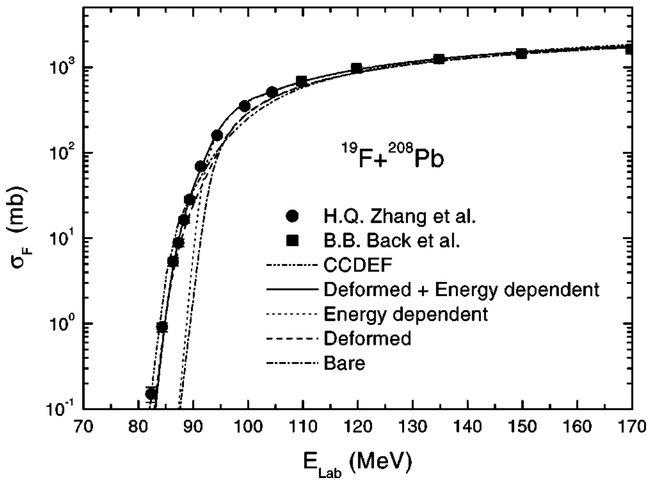

FIG. 7. The fusion excitation function for the ^{19}F+^{208}Pb system. The dash-dot-dotted line is the CC result, and solid, dotted, dashed, and dash-dotted curves are the BPM calculations with deformed plus energy dependent, only energy dependent, only deformed, and bare potentials, respectively. The circle and square data are taken from Refs. [18] and [17], respectively.

B. Fusion excitation function and spin distribution

In general, the energy dependent BPM model can reproduce the enhancement of fusion cross sections near and below the barrier well, but fails to describe the broadening of spin distribution. In addition to the energy dependence, the deformation effects are considered in the present work as mentioned in Sec. III C. The TA parameters extracted from elastic scatterings are employed in the calculations. The results reproduce both cross sections and mean-square spins well, as shown in Figs. 7 and 8, respectively. The CC results calculated by CCDEF code are also illustrated in the figure for comparison. In the CC calculation, six inelastic channels are included, as done by Zhang *et al.* [18], the 0.19714, 1.3457, 1.5540, and 2.7798 MeV excited states of ^{19}F with $\beta_2=0.55$, $\beta_3=0.33$, $\beta_2=0.58$, $\beta_4=0.22$, as well as the 2.6146 and 3.1977 MeV excited states of ^{208}Pb with $\beta_3=0.12$ and $\beta_5=0.05$, respectively. It is clear that the increases of fusion cross sections and mean-square spins around the Coulomb barrier can be attributed to the energy dependent potential, in other words, to the dynamic polarization effects. While in the energy region further below the barrier, the static deformations of the nucleus should be considered to play an important role. The small bump around the barrier in the mean-square spin distribution results from the deformations (see Fig. 8). In comparison with the calculations, we can see a slight shift of Zhang's $\langle l^2\rangle$ data which are extracted from the anisotropies of fission fragments

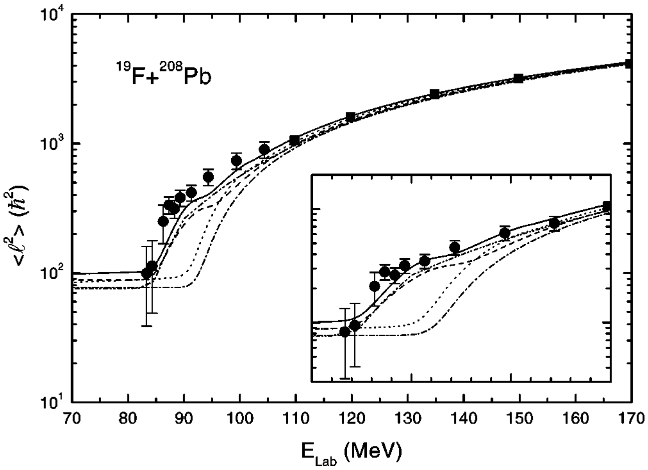

FIG. 8. Same as in Fig. 7, but for the mean-square spin distributions. Zhang's data [18] divided by 1.2 are shown in the inset.

$$A=1+\frac{\langle l^2\rangle}{4K_0^2}, \tag{19}$$

where A is the experimental anisotropies of fission fragments and K_0 is the standard deviation of the K distribution deduced from the Sierk model [23] or from systematics [24]. We conjecture that the deviation of K_0 value may cause such uniform shift in $\langle l^2\rangle$. If the data are reduced by a factor of 1.2, they agree with the calculations quite well (see the inset in Fig. 8).

V. SUMMARY

The angular distributions of elastic scatterings at six energies near and below the Coulomb barrier for ^{19}F+^{208}Pb system are presented. The phenomenological optical model analysis gives the depths of the real and imaginary potentials, showing that both real and imaginary potentials have pronounced energy dependence. The real parts of potentials derived from the fusion channel also show the energy dependence and are quite similar to those from the elastic channel. In the framework of the linear model, the TA parameters are extracted from both elastic and fusion channels. Comparison with the neighboring systems shows that the projectile deformations have effects on the fusion reaction at low energy. Using the TA parameters extracted from the elastic channels, the fusion excitation function and the mean-square spin distribution are reproduced by the deformed and energy dependent BPM model. In addition, the calculations indicate that the dynamic polarization effects play roles around the barrier, while the static deformations are at work at energies further below the barrier.

ACKNOWLEDGMENTS

We thank the operating staffs of the HI-13 tandem accelerator at CIAE for the good beams. This work was supported by the Nuclear Industry Science Foundation of China under Contract No. 92A01010.

---

[1] M. A. Nagarajan, C. C. Mahaux, and G. R. Satchler, Phys. Rev. Lett. **54**, 1136 (1985).
[2] C. Mahaux, H. Ngô, and G. R. Satchler, Nucl. Phys. **A449**, 354 (1986).
[3] G. R. Satchler, Phys. Rep. **199**, 147 (1991).
[4] C. H. Dasso, S. Landowne, and G. Pollarolo, Phys. Lett. B **217**, 25 (1989).
[5] R. Vandenbosh, Annu. Rev. Nucl. Part. Sci. **42**, 447 (1992).
[6] D. Ackermann, B. B. Back, R. R. Betts, M. Carpenter, L. Corradi, S. M. Fischer, R. Ganz, S. Gil, G. Hackman, D. J. Hofman, R. V. F. Janssens, T. L. Khoo, G. Montagnoli, V. Nanal, F. Scarlassara, M. Schlapp, D. Sewerynaik, A. M. Stefanini, and A. H. Wuosmaa, Nucl. Phys. **A630**, 442c (1998).
[7] N. Rowley, G. R. Satchler, and P. H. Stelson, Phys. Lett. B **254**, 25 (1991).
[8] J. X. Wei, J. R. Leigh, D. J. Hinde, J. O. Newton, R. C. Lemmon, S. Elfstrom, and J. X. Chen, Phys. Rev. Lett. **67**, 3368 (1991).
[9] A. M. Stefanini, J. Phys. G **23**, 1401 (1997).
[10] C. R. Morton, A. C. Berriamn, M. Dasgupta, D. J. Hinde, J. O. Newton, K. Hagino, and I. J. Thompson, Phys. Rev. C **60**, 044608 (1999).
[11] H. Leucker, K. Becker, K. Blatt, W. Korsch, W. Luck, H. G. Völk, D. Fick, R. Butsch, H. J. Jänsch, H. Reich, and Z. Moroz, Phys. Lett. B **233**, 277 (1989).
[12] D. R. Tilley, H. R. Weller, C. M. Cheves, and R. M. Chasteler, Nucl. Phys. **A595**, 1 (1995).
[13] J. Raynal, *Computing as a Language of Physics* (IAEA, Vienna, 1972), p. 281.
[14] M. H. Macfarlane and S. C. Pieper, Phys. Lett. **103B**, 169 (1981).
[15] C. Y. Wong, Phys. Rev. Lett. **31**, 766 (1973).
[16] R. A. Broglia and A. Winther, *Heavy Ion Reactions* (Addison-Wesley, New York, 1991).
[17] B. B. Back, R. R. Betts, J. E. Gindler, B. D. Wilkins, S. Saini, M. B. Tsang, C. K. Gelbke, W. G. Lynch, M. A. McMahan, and P. A. Baisden, Phys. Rev. C **32**, 195 (1985).
[18] H. Q. Zhang, Z. H. Liu, J. C. Xu, K. Xu, J. Lu, and M. Ruan, Nucl. Phys. **A512**, 531 (1990).
[19] F. Videbaek, R. B. Goldstein, L. Grodzins, S. G. Steadman, T. A. Belote, and J. D. Garrett, Phys. Rev. C **15**, 954 (1977).
[20] E. Vulgaris, L. Grodzins, S. G. Steadman, and R. Ledoux, Phys. Rev. C **33**, 2017 (1986).
[21] P. Singh, S. Kailas, A. Chatterjee, S. S. Kerekatte, A. Navin, A. Nijasure, and B. John, Nucl. Phys. **A555**, 606 (1993).
[22] R. Bass, Phys. Rev. Lett. **39**, 265 (1977).
[23] A. J. Sierk, Phys. Rev. C **33**, 2039 (1986).
[24] L. C. Vaz and J. M. Alexander, Phys. Rep. **97**, 1 (1983).